

Spin Qubit Performance at the Error Correction Threshold: Advancing Quantum Information Processing Above 700 mK

S. Amitonov, A. Aprà, M. Asker, R. Bals, B. Barry, I. Bashir, E. Blokhina, P. Giounanlis, M. Harkin, P. Hanos-Puskai, I. Kriekouki, D. Leipold, M. Moras, N. Murphy, N. Petropoulos, C. Power, A. Sammak, N. Samkharadze, A. Semenov, A. Sokolov, D. Redmond, C. Rohrbacher, X. Wu¹

¹Equal1 Laboratories

ABSTRACT

This paper presents a characterization of a two-qubit processor in a 6-quantum dot array in SiGe, from the perspective of its quantum information processing capabilities. The analysis includes randomized benchmarking of single- and two-qubit gates, SPAM characterization, and Bell's state tomography; all basic functionality required for universal quantum computation. In light of our efforts to combine spin qubits with integrated cryogenic electronics, we evaluate the qubits' performance metrics at 300 mK and 740 mK. The latter temperature lies within the realistic thermal budget for integrated cryogenic electronics, making it particularly relevant for assessing qubit performance in practical scenarios.

Introduction

Spin qubits in gate-defined quantum dots have emerged as a leading platform for scalable quantum computing, offering long coherence times, a small footprint, and compatibility with industrial semiconductor processes¹⁻⁶. Among these, Si/SiGe qubits with micromagnets stand out, with SiGe spacers isolating qubits from noisy oxide interfaces and micromagnets enabling fast driving, addressable readout, and efficient CZ gates. SiGe spin qubit systems achieve qubit operation and readout fidelities beyond the error correction threshold^{2,3,7}. They support the largest universal multi-spin qubit processors and demonstrate significant advances in operation and quantum information processing^{1,2,8}. Additionally, promising methods for intermediate and long-distance qubit connectivity through single electron shuttlers^{9,10} and microwave resonators¹¹, underline their potential for modular and scalable architectures.

Scaling these systems to utility scale will require integration of control electronics¹²⁻¹⁵, ideally co-packaged with qubits in a single System-on-Chip to minimize latency and leverage high-density 3D interconnects. However, this integration introduces significant thermal constraints¹³, imposing a temperature limit below which operation becomes impractical. Therefore, it is crucial to raise the operating temperature of these devices while ensuring that individual qubit error rates are as low as possible. Our aim is to have the total combined sources of qubit error, per gate operation, to result in a bit-flip or phase-flip error much less than 1% of the time. This target is driven by the expectation that, long term, quantum error correction will be required to reduce error rates to practical levels. A popular and implementable scheme¹⁶⁻¹⁸, the rotated surface code, has a relatively forgiving "threshold" error rate of 1%, below which qubit errors are corrected more and more efficiently¹⁹.

In this work, we investigate two physical qubits in a 6-quantum dot array in Si/SiGe at two temperatures, 300 mK and 740 mK. We calibrate and benchmark a universal native gate set for a two-qubit processor, and perform Bell state tomography. Extracted single- and two-qubit fidelities do not show a significant decline with increasing temperature, with qubits performing at the error correction threshold at both temperatures. However, at the higher temperature, state preparation and measurement (SPAM) errors increase due to reduced sensitivity of the single electron transistor used for readout. Correcting for SPAM, we construct a Bell state with over 98.5% fidelity at both temperatures.

Bell state preparation, which generates a maximally entangled two-qubit state, along with state tomography and a SPAM correction scheme, are critical components for quantum information processing in this system. Demonstrating these capabilities at elevated temperatures represents a significant milestone in advancing the SiGe platform's practical utility.

Finally, we note that our qubits operate below 5 GHz, a comfortable frequency range for integration with widely-used RF technologies found in handheld and embedded devices, such as PLLs and CMOS-based RF synthesizers and realizable with commercial semiconductor processes.

System Outline

A false-colored SEM image of our device is presented in Fig. 1 a). The structure consists of two Single Electron Transistors (SET) and an array with up to 6 quantum dots, made by 6 plunger (P) gates to control the dots confinement and 7 tunneling T gates to control interdot and dot-sensor tunnel barriers. In the inset of Fig. 1 a), the calculated conduction band edge is shown at a xy -plane slice taken in the middle of the conduction channel. We simulated our six-quantum-dot array, along with the two sensing devices located at each side, using the Quantum Technology Computer Aided Design (QTCAD) finite element simulation (FEM) tool²⁰. The device 3D geometry was defined via the FEM mesh generator Gmsh²¹, which produced a first-order mesh consisting of 6500 nodes. Localized refinements were applied in the conduction channel region to improve precision and ensure convergence. Isothermal conditions were assumed applying a uniform temperature of 300 mK across the entire device. Assuming thermodynamic equilibrium, the non-linear Poisson equation²² was solved self-consistently, calculating the electrostatic potential throughout the structure as well as the corresponding classical charge distribution. Quantum dots are formed at the energy minima, the energy levels of which are controlled by modifying the voltage applied on the plunger gates, while the height and width of the barriers between adjacent dots are controlled by adjusting the biases of the tunneling gates.

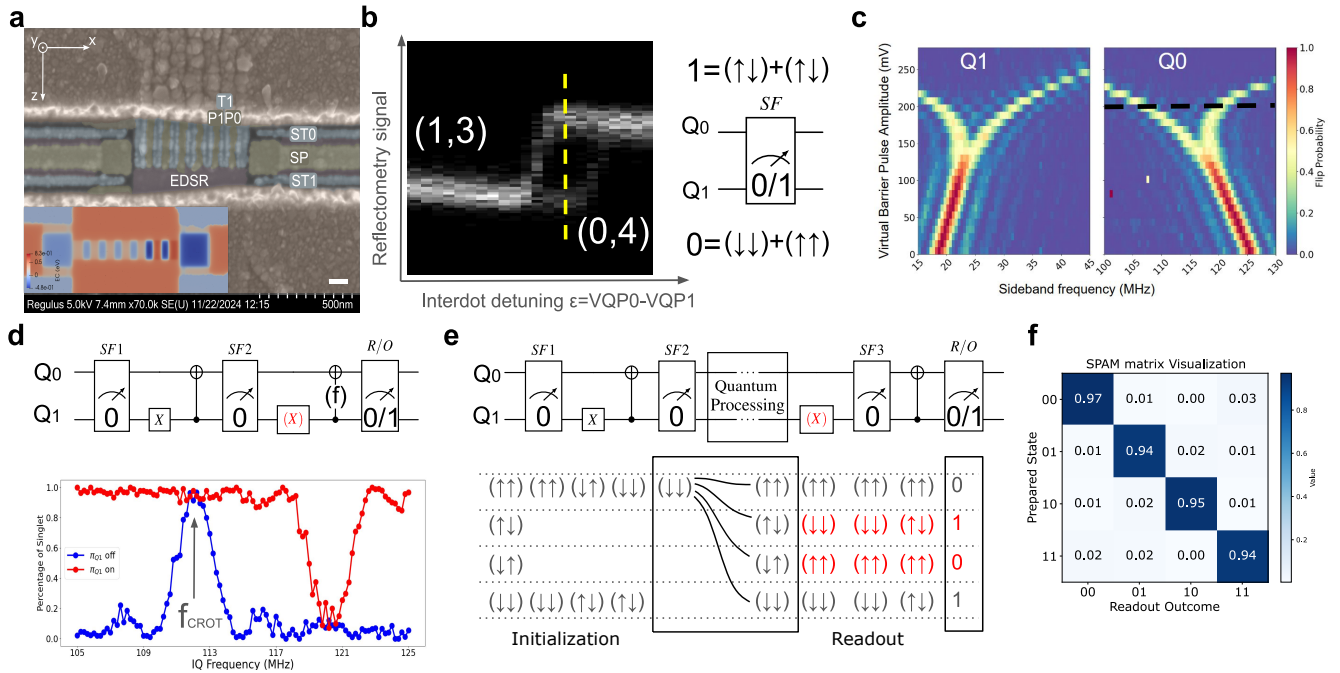


Figure 1. a) Scanning electron micrograph of a 6-quantum dot device nominally identical to the one measured. The inset shows a QTCAD simulation of the confinement potential profile. b) Histogram of the charge sensor signal as a function of the detuning ϵ , scanning perpendicularly to interdot charge transition. The yellow dashed line identifies the readout point, where parity readout is enabled. c) Q_1 and Q_0 frequencies (left and right plot, respectively) as a function of virtual barrier pulse amplitude. The pulse on the interdot barrier activates the exchange coupling, exhibiting the typical spin funnel shape²³. d) Demonstration of CROT gate. Following a double initialization stage, as explained in main text, a CROT is applied on target qubit Q_0 with control qubit Q_1 . We show the percentage of singlets measured with and without a π rotation on the control qubit Q_1 . The virtual barrier amplitude is approximately 220 mV, as indicated by dashed line in c). e) Initialization and readout of two qubit state. We apply an additional state filtering (SF3) followed by a CROT operation for the two-qubit readout. This allows to distinguish between two states with same parity, as shown in the schematics. By applying an additional X rotation on control Q_1 before the readout stage, SF3, we can map odd states into even states, thus enabling the readout of odd states. f) Example of a SPAM matrix for the two qubits.

Results: Metrics Details

Parity measurement-based initialization and readout of the two-qubit processor

Quantum dot transitions in the array can be probed with an RF-SET²⁴, where the sensor dot is controlled by plunger SP, and tunneling with reservoirs by tunneling gates ST_0, ST_1 (see Fig. 1a). A high impedance superconducting inductor is connected to the accumulation gate of the RF-SET²⁵.

We accumulate a double quantum dot (DQD) underneath the plunger gates QP_0 and QP_1 . In the following we refer to the corresponding qubits as Q_0 and Q_1 . After optimizing the charge sensor dot, the tunnel barriers controlled by gates QT_0 , QT_1 are then tuned to bring the DQD into a regime suitable for Pauli Spin Blockade (PSB).

In Fig. 1(b) we report the histogram of a charge sensor signal while scanning the detuning axis $\varepsilon = V_{QP_0} - V_{QP_1}$. The yellow dashed line indicates the chosen readout point. At such a readout point we can observe parity-dependent tunneling. This allows to filter the parity of the initial states by adding an additional readout/state filtering stage (SF1) and therefore to work only with states of known parity. In the circuit diagrams we label even states as 0 and odd states as 1.

The spin manipulation is enabled by the gradient of a micromagnet field that generates a "synthetic" spin-orbit coupling²⁶. The micromagnet field is maximized on qubit Q_0 and becomes lower as we move further along the qubit array. Fig. 1(c) shows the effect of exchange coupling on the two qubit resonant frequencies. The visible slope of the resonances is due to the fact that increasing the barrier pulse amplitude decreases the distance between the two dots, and they therefore experience a differing static field due to the micromagnet. The splitting of the two lines is directly related to the magnitude of J coupling. Each of the resonances is activated depending on the state of the other qubit. This allows to perform conditional operations on the two qubit system. We note that the visibility of the two split resonances are about 50%, as the other (control) qubit is in a mixed state.

By adding a π pulse (X Pauli rotation) on control qubit Q_1 and an additional CROT after the first state filtering stage (SF1), and then filtering again (SF2), we can reliably initialize the two-qubit system in one of the two even states⁴. The two-stage initialization protocol shown prepares the system in the $|\downarrow, \downarrow\rangle$ state. Setting the state of control and target qubits leads to visibility of two qubit operations approaching 100%. The CROT operation shown in Fig. 1 d) demonstrates conditional control over the two qubit state. We show that by flipping the control qubit Q_1 another CROT operation is enabled, corresponding to the other, otherwise suppressed, branch of the spin exchange funnel.

The CROT also allows to discriminate between two states of the same parity via a double readout stage. The CROT operation is repeated after the readout/state filtering stage (SF3) to remove the $|\uparrow, \uparrow\rangle$ state. This algorithmic procedure allows to extend parity readout to the full two-spin state basis.

This technique allows for more accurate initialization, with accuracy mainly limited by the CROT operation, at the cost of discarding many unwanted states. A real time feedback technique^{1,27} would allow to initialize quasi-deterministically all 4 two-spin states, thus increasing the speed of the quantum processor.

Next we characterize qubit performance at two different temperatures. Fig.2 a) shows Ramsey fringes used to extract coherence times of the two qubits. Here we do see a reduction in T_2^* more than a factor of 2 as the temperature increases. However, the experiments at the two temperatures differed quite substantially in their duration, 8 minutes at 300 mK versus 80 minutes at 740 mK. Thus it is not the fairest comparison, as the longer experiment suffers more from $1/f$ charge noise, which is believed to be the dominant contributor to decoherence²⁸. We obtain pure dephasing times of $T_2^* > 10 \mu s$ at $T=300 mK$, and $T_2^* > 4 \mu s$ at $T=740 mK$, extended to $T_2^{ECHO}=70 \mu s$ and $T_2^{ECHO}=40 \mu s$ with Hahn echo (See supplementary Fig. 6).

Single qubit randomized benchmarking

To find the fidelity of one qubit gates we have used a standard technique of Clifford randomized benchmarking (RB)²⁹. The protocol was performed within the $\{I, X(\pm \frac{\pi}{2}), Z(\pm \frac{\pi}{2}), X(\pm \pi), Z(\pm \pi)\}$ native gate-set, with the so-called virtual Z gate implemented as a phase shift³⁰. The virtual Z gate allows for a near perfect implementation of the Z gate with zero-duration, greatly improving the one-qubit gate fidelity. Each Clifford gate was compiled into a circuit with an average of 0.83 one-qubit X rotations. We sample N random sequences for each Clifford gate depth d and M shots per measurement. The average values for each Clifford depth are fitted with $W = Ab^d + c$, where A , b and c are fitting parameters, and the fidelity is calculated as $F = (1 + b)/2$. The experimental results and their fits are shown in the Fig. 2(b) where we give the results of the benchmarking. The error bars designate standard deviation over the random Clifford sequences.

Two-qubit Interleaved Character Randomized Benchmarking for CZ

We characterize the fidelity of our native entangler CZ using the interleaved character benchmarking procedure. The standard interleaved randomized benchmarking technique³¹, when extended to two qubit gates, results in relatively deep (3.9 one qubit non-virtual gates and 1.48 CZ gates per Clifford), circuits in our native gate set, $\{I, X(\pm \frac{\pi}{2}), Z(\pm \frac{\pi}{2}), X(\pm \pi), Z(\pm \pi), CZ\}$. This leads to a fast decay in the resulting benchmarking curve giving low predictions of two-qubit gate fidelity with large uncertainty. In this work we use instead a technique called interleaved character randomized benchmarking (ICRB)³². ICRB allows one to calculate the fidelity of a two qubit gate using finite groups other than the Clifford group (for the technical details of the method see³³). Within ICRB one chooses a benchmarking group and a character group. Whilst the benchmarking group plays the same role as in the standard RB, it is the additional character group that allows the freedom of choice in the benchmarking group (for the standard RB, the benchmarking group is fixed to n -qubit Clifford group $Clif_n$). By careful choice of the benchmarking and character groups within the ICRB one can avoid noise accumulation by exploiting high-fidelity gates and concentrating on the

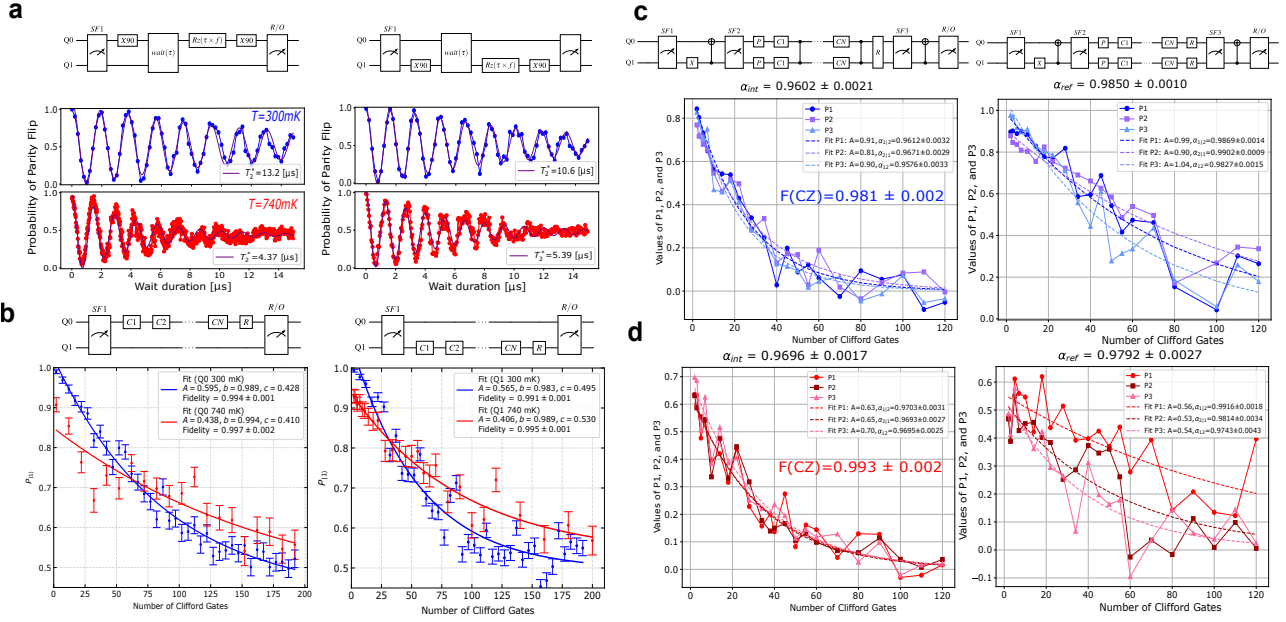


Figure 2. Benchmarking qubit fidelities at two different temperatures. a) Ramsey interference fringes for Q_0 and Q_1 at $T=300$ mK and $T=740$ mK. Free induction decay rate is extracted from decaying spin fits to the data, with total measurement time of 8 minutes at $T=300$ mK and 2 hours at $T=740$ mK. b) Clifford randomized benchmarking for both qubits (Q_0 on the left and Q_1 on the right) at temperatures of 300mK (blue) and 740mK (red). Each datapoint represents an average return probability after applying 25 random Clifford sequences per circuit length, with the standard deviation shown with error bars. Data is fit with an exponential decay, with errors for Clifford fidelity numbers extracted from fit deviation. c) and d) show the interleaved character randomized benchmarking of the CZ gate at $T = 300$ mK and $T = 700$ mK respectively. The CZ operations are interleaved by single qubit Clifford operations, while the reference benchmarking is shown on the right in both c) and d).

target gate. For the spin-based qubits, it is convenient³² to choose a product of two one-qubit Clifford groups $\text{Clif}_1 \otimes \text{Clif}_1$, and a two-qubit Pauli group \mathcal{P}_2 as a character group. The protocol for the ICRB within the chosen groups is as follows:

1. Initialize a two-qubit system in one of the computational basis states $|s_1s_2\rangle \in \mathcal{B} = \{|00\rangle, |01\rangle, |10\rangle, |11\rangle\}$, by applying a random one qubit Pauli from \mathcal{P}_2 .
2. Apply to each of the qubits a random one-qubit Clifford gate. Do this d times.
3. Apply the inverse Clifford gate C_{inv} to each qubit. The inverse gate does not include the initial Pauli gate.
4. For each basis set measure $P_d(s_1s_2) = |\langle 00|C_{inv}S_d|s_1s_2\rangle|^2$, which are the probabilities of measuring $|00\rangle$ for a given sampled Clifford sequence S_d for each initialization $|s_1s_2\rangle$.
5. Calculate for each measured P_d :

$$\begin{aligned}
 P_d^{(1)} &= P_d(00) - P_d(01) + P_d(10) - P_d(11), \\
 P_d^{(2)} &= P_d(00) + P_d(01) - P_d(10) - P_d(11), \\
 P_d^{(3)} &= P_d(00) - P_d(01) - P_d(10) + P_d(11).
 \end{aligned}$$

6. Fit each of the results using

$$\begin{aligned}
 P_1 &= A_1 \alpha_{1|2}^m, \\
 P_2 &= A_2 \alpha_{2|1}^m, \\
 P_3 &= A_3 \alpha_{12}^m.
 \end{aligned}$$

7. Calculate $\alpha_{ref} = (\alpha_{1|2} + \alpha_{2|1} + 3\alpha_{12})/5$.

8. Perform the previous steps, interleaving one-qubit Clifford gates at step 2 with CZ, and calculate α_{int} in the same way.
9. Calculate fidelity $F = 1 - (1 - \frac{\alpha_{int}}{\alpha_{ref}})^{\frac{3}{4}}$.

The results of this protocol are given in the Fig. 2(c) and (d) for 300 mK and 740 mK, respectively.

Bell state tomography and SPAM characterization

To verify entanglement in our system, we perform full state tomography on the Bell state $|\Phi\rangle = \frac{1}{\sqrt{2}}(|00\rangle + |11\rangle)$. Our reconstruction of the density matrix is based on the Pauli decomposition of its density matrix $\rho = \sum_{\sigma \in P_2} c_{\sigma} \sigma$, where $P_2 = \{I, \sigma_x, \sigma_y, \sigma_z\}^{\otimes 2}$ and $c_{\sigma} = \langle \sigma \rangle / 4$ are a set of all two-qubit Pauli matrix combinations and a normalized expectation value of a two-qubit Pauli operator σ , respectively. The latter we find by measuring expectation values of all 16 two-qubit Pauli strings. The resulting density matrices $T = 300$ mK and 740 mK are visualized in Fig. 3(a) and (c), respectively. The fidelity, concurrence, and Frobenius distance from the expected state $|\Phi\rangle$ are given in the Table 1. The explicit density matrices are given in Table 3.

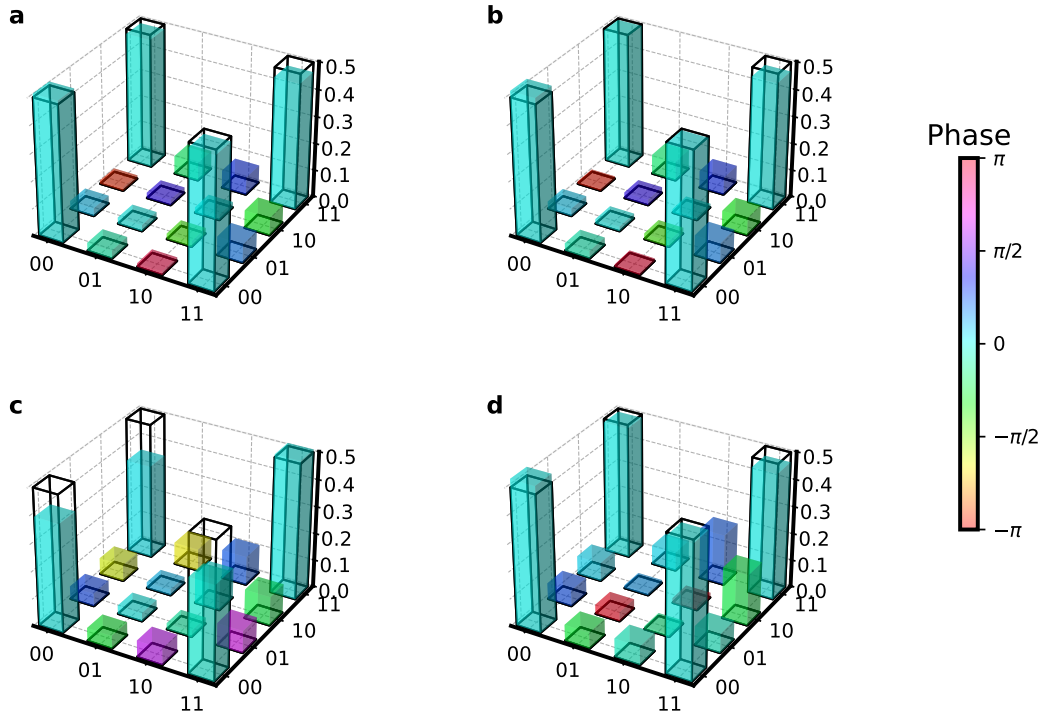


Figure 3. Reconstructed density matrices for the Bell state $\frac{1}{\sqrt{2}}(|00\rangle + |11\rangle)$. Color indicates phase. $T = 300$ mK: (a) reconstructed density matrix via full tomography, (b) SPAM corrected density matrix. $T = 740$ mK: (c) reconstructed density matrix, (d) SPAM corrected density matrix. The fidelity, concurrence, Frobenius distance from the pure state and a trace are given in Table 1. The black wireframe indicates where the bars would be ideally.

	$T = 300$ mK		$T = 740$ mK	
	no SPAM correction	with SPAM correction	no SPAM correction	with SPAM correction
Fidelity	0.977	0.989	0.799	0.985
Concurrence	0.808	0.827	0.587	0.751
Frobenius distance	0.065	0.066	0.245	0.159
Trace	1.022	1.021	1.051	0.942

Table 1. Tomography results for the two-qubit Bell state $|\Phi\rangle = \frac{1}{\sqrt{2}}(|00\rangle + |11\rangle)$.

Immediately after the tomography measurements, the SPAM confusion matrix was measured using the following scheme: the system was prepared in every state in the computational basis set $\mathcal{B} = \{|00\rangle, |01\rangle, |10\rangle, |11\rangle\}$, and for each state $|i_1 i_2\rangle \in \mathcal{B}$

the probabilities $P(r_1 r_2 | i_1 i_2)$ of being in the state $|r_1 r_2\rangle \in \mathcal{B}$ were measured. The SPAM matrices used are given in Table 4. We have used these results to mitigate the SPAM noise for the Bell’s state tomography results (see Fig. 3(c) and (d) and Table 1).

Discussion

We summarize measured physical properties of the qubits and the performance of the two-qubit processor at both temperatures in Table 2.

Qubit	frequency	T_1	T_2^*	T_2^{echo}	X90	CZ180	1Q F_{Clif}	2Q F_{CZ}	Bell state fidelity Raw (SPAM corr.)
Q_0 @ 300 mK	4.48 GHz	$\gtrsim 380$ ms	$13.2 \mu\text{s}$	-	84 ns	96 ns	99.4%	$98.1 \pm 0.2\%$	97.7% (98.9%)
Q_1 @ 300 mK	4.59 GHz	$\gtrsim 380$ ms	$10.6 \mu\text{s}$	$70 \mu\text{s}$	112 ns	96 ns	99.1%		
Qubit	frequency	T_1	T_2^*	T_{ECHO}^2	X90	CZ180	1Q F_{Clif}	2Q F_{CZ}	Bell state fidelity Raw (SPAM corr.)
Q_0 @ 740 mK	4.48 GHz	$\gtrsim 65$ ms	$4.4 \mu\text{s}$	$41 \mu\text{s}$	84 ns	96 ns	99.7%	$99.3 \pm 0.2\%$	80% (98.5%)
Q_1 @ 740 mK	4.59 GHz	$\gtrsim 65$ ms	$5.4 \mu\text{s}$	$46 \mu\text{s}$	108 ns	96 ns	99.5%		

Table 2. Summary of qubit metrics.

The relaxation rate increases dramatically as expected with higher temperatures; however, we still observe a relatively long T_1 of 65 ms at 740 mK, which remains negligible compared to other relevant timescales. Interestingly, despite the reduction in dephasing times, fidelities derived from randomized benchmarking (RB) sequences do not reduce, and even show improvement as the temperature increases from 300 mK to 740 mK. In contrast, SPAM-corrected Bell state fidelities exhibit a modest decline at the elevated temperature.

These observations suggest that the overall qubit performance is not monotonically affected by temperature changes but rather reflects a balance between competing effects. Low-frequency noise likely increases at higher temperatures, adversely impacting T_2^* and Bell state fidelity, which are more sensitive to such noise. Randomized benchmarking and interleaved RB, which involve long sequences of single-qubit gates, effectively decouple low-frequency noise. Additionally, microwave-induced heating is known to alter qubit properties^{7,34}, an effect that decreases with increased temperature³⁵. Randomized benchmarking measurements are more sensitive to such changes, potentially accounting for the observed fidelity improvements at high temperatures.

In conclusion, spin qubits in SiGe perform well at elevated temperatures above 700 mK, nearing the quantum error correction threshold. An increase in SPAM errors is observed, primarily due to the limitations of traditional SETs, which rely on the sharpness of the Fermi level in the reservoirs. To address these limitations at higher temperatures, alternative charge sensors—such as gate sensors with superconducting inductors³⁶ and double dot SETs³⁷ offer promising solutions by sensing interdot transitions directly.

In the future, we will focus on extending the operational temperature range of charge sensors in qubit arrays and integrating the qubits with our fifth-generation control chip. The control chip supports a programmable qubit control system with integrated neural network feedback loop for enhanced error correction performance, fully programmable pattern and RF synthesis engine, ARM based sequencing and scheduling core, all designed to work at compatible cryogenic temperature with integrated qubits or external SiGe qubits dies in a 3D package configuration.

Methods

Device fabrication

Devices are fabricated on an undoped $^{28}\text{Si}/\text{SiGe}$ heterostructure featuring an 7 nm strained ^{28}Si quantum well, with a residual Si concentration of 0.08%, grown on a strain-relaxed $\text{Si}_{0.7}\text{Ge}_{0.3}$ buffer layer. The quantum well is separated from the surface by a 30 nm thick $\text{Si}_{0.7}\text{Ge}_{0.3}$ spacer, terminated by a Si-rich passivation layer³⁸. The gate stack consists of 3 layers of Ti:Pd metallic gates (3:17, 3:27, 3:27 nm) isolated from each other by 5 nm Al_2O_3 dielectrics, deposited using atomic layer deposition. A ferromagnetic Ti:Co (5:200 nm) layer on top of the gate stack creates a local magnetic field gradient for qubit addressing and manipulation. Further details of device fabrication methods can be found at³⁹.

Acknowledgements

We acknowledge the Netherlands Organisation for Applied Scientific Research (TNO) and its Quantum Information Technology Test (QITT) group for their valuable contributions, support, and the discussions that stimulated the development of this work.

References

1. Philips, S. G. J. *et al.* Universal control of a six-qubit quantum processor in silicon. *Nature* **609**, 919–924, DOI: [10.1038/s41586-022-05117-x](https://doi.org/10.1038/s41586-022-05117-x) (2022).
2. Noiri, A. *et al.* Fast universal quantum gate above the fault-tolerance threshold in silicon. *Nature* **601**, 338–342 (2022).
3. Mills, A. R. *et al.* Two-qubit silicon quantum processor with operation fidelity exceeding 99%. *Sci. Adv.* **8**, eabn5130, DOI: [10.1126/sciadv.abn5130](https://doi.org/10.1126/sciadv.abn5130) (2022). <https://www.science.org/doi/pdf/10.1126/sciadv.abn5130>.
4. Huang, J. Y. *et al.* High-fidelity spin qubit operation and algorithmic initialization above 1 k. *Nature* **627**, 772–777, DOI: [10.1038/s41586-024-07160-2](https://doi.org/10.1038/s41586-024-07160-2) (2024).
5. Zwerver, A. M. J. *et al.* Qubits made by advanced semiconductor manufacturing. *Nat. Electron.* **5**, 184–190, DOI: [10.1038/s41928-022-00727-9](https://doi.org/10.1038/s41928-022-00727-9) (2022).
6. Weinstein, A. J. *et al.* Universal logic with encoded spin qubits in silicon. *Nature* **615**, 817–822, DOI: [10.1038/s41586-023-05782-0](https://doi.org/10.1038/s41586-023-05782-0) (2023). 19k accesses, 40 citations, 117 Altmetric.
7. Xue, X. *et al.* Quantum logic with spin qubits crossing the surface code threshold. *Nature* **601**, 343–347 (2022).
8. Takeda, K. *et al.* Rapid single-shot parity spin readout in a silicon double quantum dot with fidelity exceeding 99%. *npj Quantum Inf.* **10**, 22, DOI: [10.1038/s41534-024-00813-0](https://doi.org/10.1038/s41534-024-00813-0) (2024).
9. Seidler, I. *et al.* Conveyor-mode single-electron shuttling in si/sige for a scalable quantum computing architecture. *npj Quantum Inf.* **8**, 100, DOI: [10.1038/s41534-022-00620-y](https://doi.org/10.1038/s41534-022-00620-y) (2022). Published: 30 August 2022.
10. Smet, M. D. *et al.* High-fidelity single-spin shuttling in silicon. *arXiv preprint arXiv:2406.07267* (2024). 15 pages, 15 figures.
11. Dijkema, J. *et al.* Two-qubit logic between distant spins in silicon. *arXiv preprint arXiv:2310.16805* (2023). 17 pages, 9 figures.
12. Staszewski, R. B. *et al.* Cryogenic controller for electrostatically controlled quantum dots in 22-nm quantum soc. *IEEE Open J. Solid-State Circuits Soc.* **2**, 103–121 (2022).
13. Bashir, I. *et al.* Monolithically integrated quantum dots in a 22-nm fully depleted silicon-on-insulator process operating at 3 k. *Int. J. Circuit Theory Appl.* (2024).
14. Pauka, S. *et al.* A cryogenic cmos chip for generating control signals for multiple qubits. *Nat. Electron.* **4**, 64–70 (2021).
15. Xue, X. *et al.* Cmos-based cryogenic control of silicon quantum circuits. *Nature* **593**, 205–210 (2021).
16. Krinner, S. *et al.* Realizing repeated quantum error correction in a distance-three surface code. *Nature* **605**, 669–674, DOI: [10.1038/s41586-022-04566-8](https://doi.org/10.1038/s41586-022-04566-8) (2022).
17. Acharya, R. *et al.* Suppressing quantum errors by scaling a surface code logical qubit. *Nature* **614**, 676–681, DOI: [10.1038/s41586-022-05434-1](https://doi.org/10.1038/s41586-022-05434-1) (2023).
18. Bluvstein, D. *et al.* Logical quantum processor based on reconfigurable atom arrays. *Nature* **626**, 58–65, DOI: [10.1038/s41586-023-06927-3](https://doi.org/10.1038/s41586-023-06927-3) (2024).
19. Horsman, C., Fowler, A. G., Devitt, S. & Van Meter, R. Surface code quantum computing by lattice surgery. *New J. Phys.* **14**, 123011, DOI: [10.1088/1367-2630/14/12/123011](https://doi.org/10.1088/1367-2630/14/12/123011) (2012). ArXiv:1111.4022 [quant-ph].
20. QTCAD: A Computer-Aided Design Tool for Quantum-Technology Hardware, Nanoacademic Technologies Inc. (2022).
21. Geuzaine, C. & Remacle, J.-F. Gmsh: A 3-d finite element mesh generator with built-in pre- and post-processing facilities. *Int. J. for Numer. Methods Eng.* **79**, 1309–1331, DOI: [10.1002/nme.2579](https://doi.org/10.1002/nme.2579) (2009).
22. Gao, S. A quantum theory of consciousness. *Minds Mach.* **18**, 39–52, DOI: [10.1007/s11023-007-9084-0](https://doi.org/10.1007/s11023-007-9084-0) (2007).
23. Petta, J. R. *et al.* Coherent manipulation of coupled electron spins in semiconductor quantum dots. *Science* **309**, 2180–2184, DOI: [10.1126/science.1116955](https://doi.org/10.1126/science.1116955) (2005). <https://www.science.org/doi/pdf/10.1126/science.1116955>.
24. Vigneau, F. *et al.* Probing quantum devices with radio-frequency reflectometry. *Appl. Phys. Rev.* **10**, DOI: [10.1063/5.0088229](https://doi.org/10.1063/5.0088229) (2023).
25. Liu, Y.-Y. *et al.* Radio-frequency reflectometry in silicon-based quantum dots. *Phys. Rev. Appl.* **16**, 014057, DOI: [10.1103/PhysRevApplied.16.014057](https://doi.org/10.1103/PhysRevApplied.16.014057) (2021).
26. Pioro-Ladrière, M. *et al.* Electrically driven single-electron spin resonance in a slanting zeeman field. *Nat. Phys.* **4**, 776–779, DOI: [10.1038/nphys1053](https://doi.org/10.1038/nphys1053) (2008).

27. Kobayashi, T. *et al.* Feedback-based active reset of a spin qubit in silicon. *npj Quantum Inf.* **9**, 52, DOI: [10.1038/s41534-023-00719-3](https://doi.org/10.1038/s41534-023-00719-3) (2023).
28. Kha, A., Joynt, R. & Culcer, D. Do micromagnets expose spin qubits to charge and johnson noise? *Appl. Phys. Lett.* **107**, 172101, DOI: [10.1063/1.4934693](https://doi.org/10.1063/1.4934693) (2015). https://pubs.aip.org/aip/apl/article-pdf/doi/10.1063/1.4934693/13149626/172101_1_online.pdf.
29. Magesan, E., Gambetta, J. M. & Emerson, J. Characterizing quantum gates via randomized benchmarking. *Phys. Rev. A* **85**, 042311, DOI: [10.1103/PhysRevA.85.042311](https://doi.org/10.1103/PhysRevA.85.042311) (2012).
30. McKay, D. C., Wood, C. J., Sheldon, S., Chow, J. M. & Gambetta, J. M. Efficient Z gates for quantum computing. *Phys. Rev. A* **96**, 022330, DOI: [10.1103/PhysRevA.96.022330](https://doi.org/10.1103/PhysRevA.96.022330) (2017).
31. Magesan, E. *et al.* Efficient measurement of quantum gate error by interleaved randomized benchmarking. *Phys. Rev. Lett.* **109**, 080505, DOI: [10.1103/PhysRevLett.109.080505](https://doi.org/10.1103/PhysRevLett.109.080505) (2012).
32. Xue, X. *et al.* Benchmarking gate fidelities in a Si/SiGe two-qubit device. *Phys. Rev. X* **9**, 021011, DOI: [10.1103/PhysRevX.9.021011](https://doi.org/10.1103/PhysRevX.9.021011) (2019).
33. Helsen, J., Xue, X., Vandersypen, L. & Wehner, S. A new class of efficient randomized benchmarking protocols. *npj Quantum Inf.* **5**, 71, DOI: [10.1038/s41534-019-0182-7](https://doi.org/10.1038/s41534-019-0182-7) (2019).
34. Takeda, K. *et al.* Optimized electrical control of a si/sige spin qubit in the presence of an induced frequency shift. *npj Quantum Inf.* **4**, 54, DOI: [10.1038/s41534-018-0104-2](https://doi.org/10.1038/s41534-018-0104-2) (2018). Published: 29 October 2018.
35. Undseth, B. *et al.* Hotter is easier: unexpected temperature dependence of spin qubit frequencies. *Phys. Rev. X* **13**, 041015 (2023).
36. Zheng, G. *et al.* Rapid gate-based spin read-out in silicon using an on-chip resonator. *Nat. Nanotechnol.* **14**, 742–746, DOI: [10.1038/s41565-019-0483-1](https://doi.org/10.1038/s41565-019-0483-1) (2019). Published: 08 July 2019, Author Correction: 25 November 2019.
37. Huang, J. Y. *et al.* A high-sensitivity charge sensor for silicon qubits above 1 k. *ACS Nano* **15**, 8097–8104, DOI: [10.1021/acsnano.1c02463](https://doi.org/10.1021/acsnano.1c02463) (2021).
38. Degli Esposti, D., Paquelet Wuetz, B., Fezzi, M., V. Lodari, Sammak, A. & Scappucci, G. Wafer-scale low-disorder 2DEG in ²⁸Si/SiGe without an epitaxial Si cap. *Appl. Phys. Lett.* **120** (2022).
39. Lawrie, W. *et al.* Quantum dot arrays in silicon and germanium. *Appl. Phys. Lett.* **116** (2020).

Supplementary

Single qubit gates

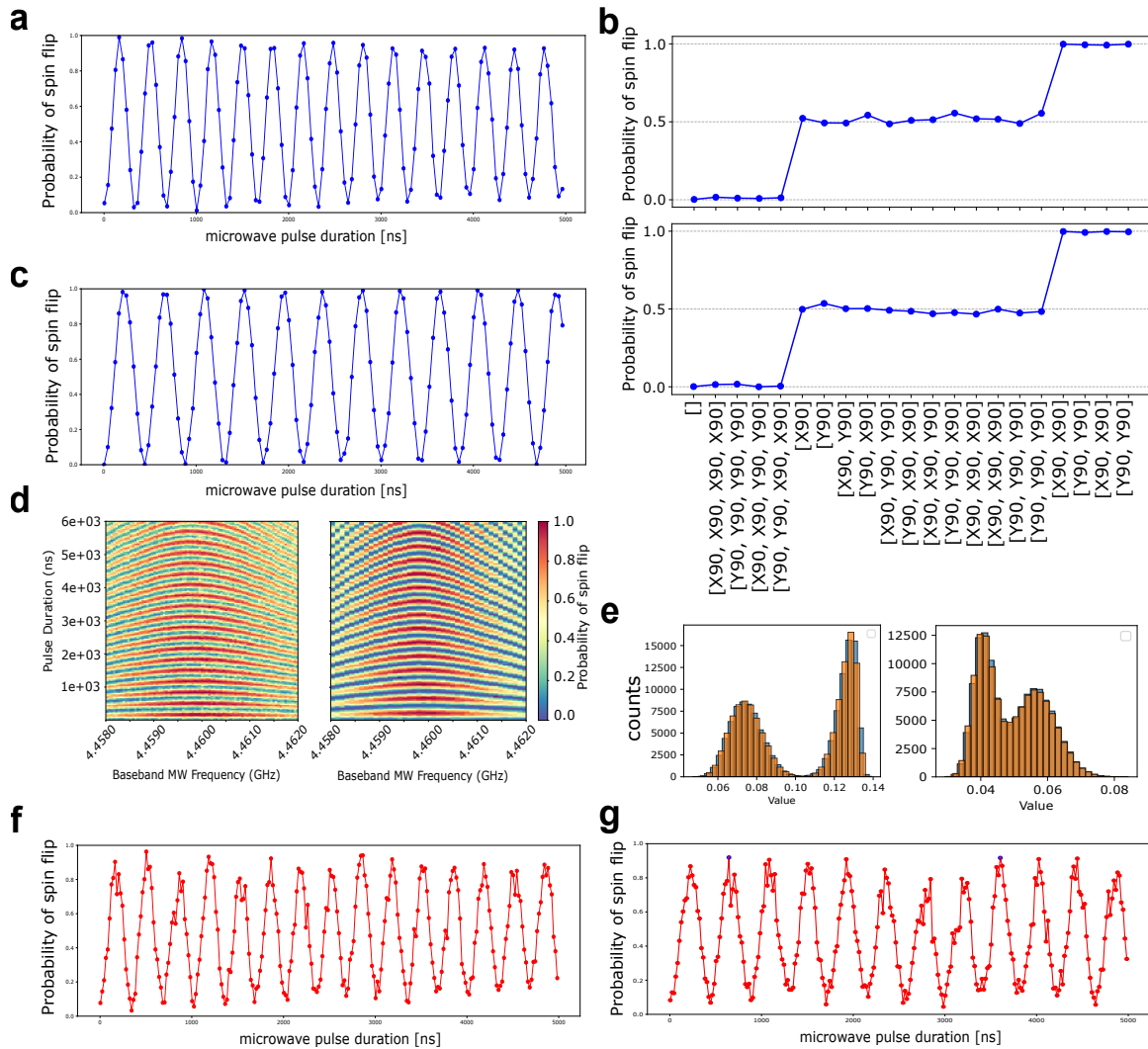


Figure 4. Single qubit gates: (a, c) Rabi oscillations of Q_0 and Q_1 at 300 mK. (b) ALLXY sequences implemented on Q_0 (top) and Q_1 (bottom). Notably visibility of X gates with single qubit readout is approaching 1(98%). (d) Chevron patterns produced with Q_0 and Q_1 . Here, IQ sideband frequency is fixed to approximately 18 MHz for Q_0 and 121 MHz for Q_1 , and the baseband frequency of the microwave source is scanned. (e) Histograms of readout signal at 300 mK (left), and 740 mK (right). (f, g) Rabi oscillations of Q_0 and Q_1 at 740 mK.

Two qubit gates

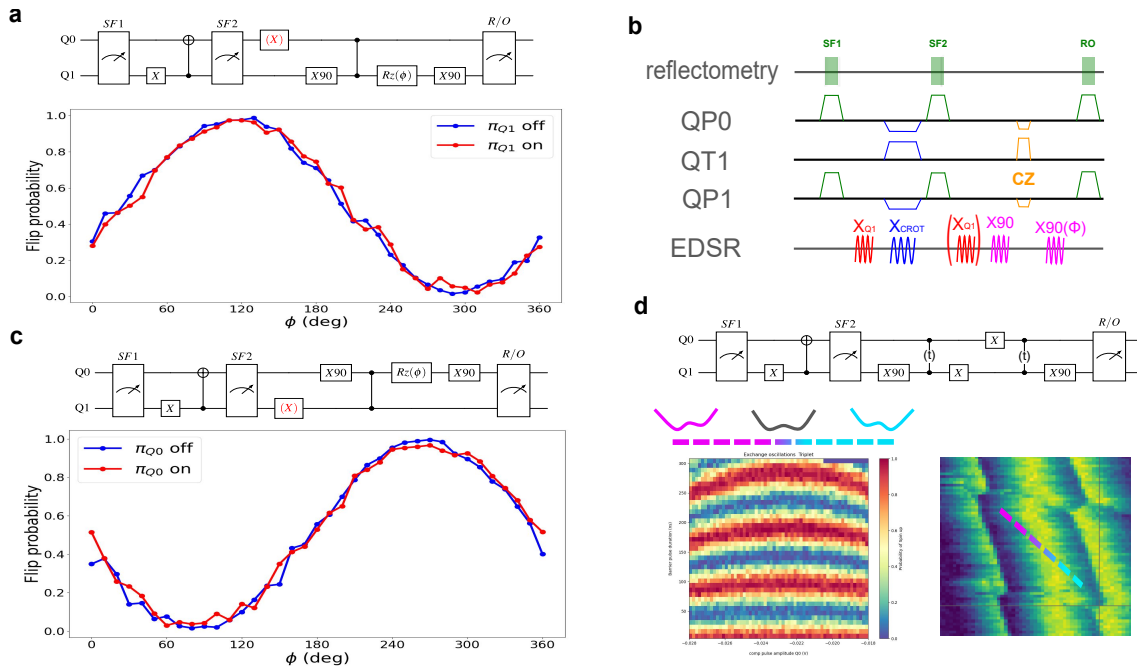


Figure 5. Two qubit gate calibration at 300 mK: (a, c) CZ phase correction calibrations for Q_0 and Q_1 respectively. (b) A diagram of voltage pulses applied to the quantum dot array electrodes, and to the reflectometry readout circuit. (d) Finding the symmetric operating point for 2 qubit exchange, using decoupled CZ sequence. On x axis, we vary the compensation pulses applied to QP₀ and QP₁ gates, gradually increasing the contribution from one and reducing from the other. We find a symmetric point in the middle, where the exchange is first order insensitive to detuning and thus suffers least from charge noise-induced decoherence.

Relaxation and Hahn echo experiments

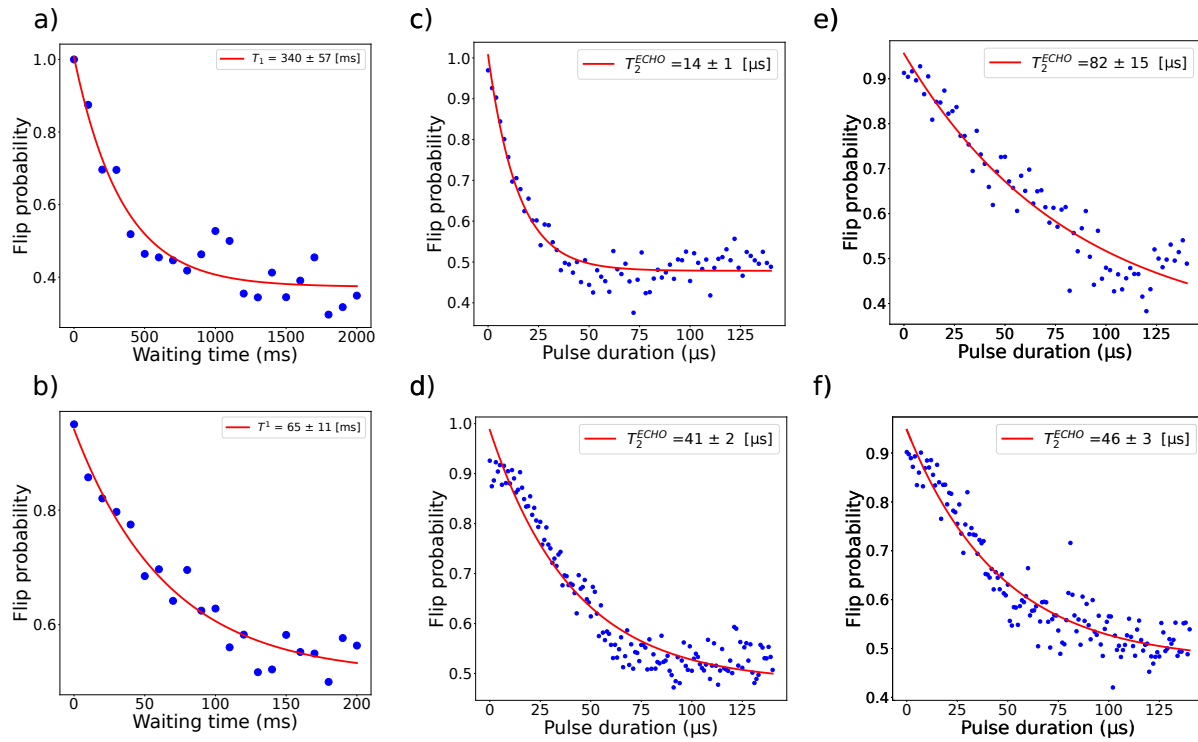


Figure 6. (a,b) Spin relaxation time T_1 measurement of antiparallel state at 300 and 740 mK, respectively. (c-d) Measurement of spin dephasing time with Hahn echo T_{ECHO}^2 measurement, at 300 and 740 mK on Q_0 . e,f) T_{ECHO}^2 of Q_1 .

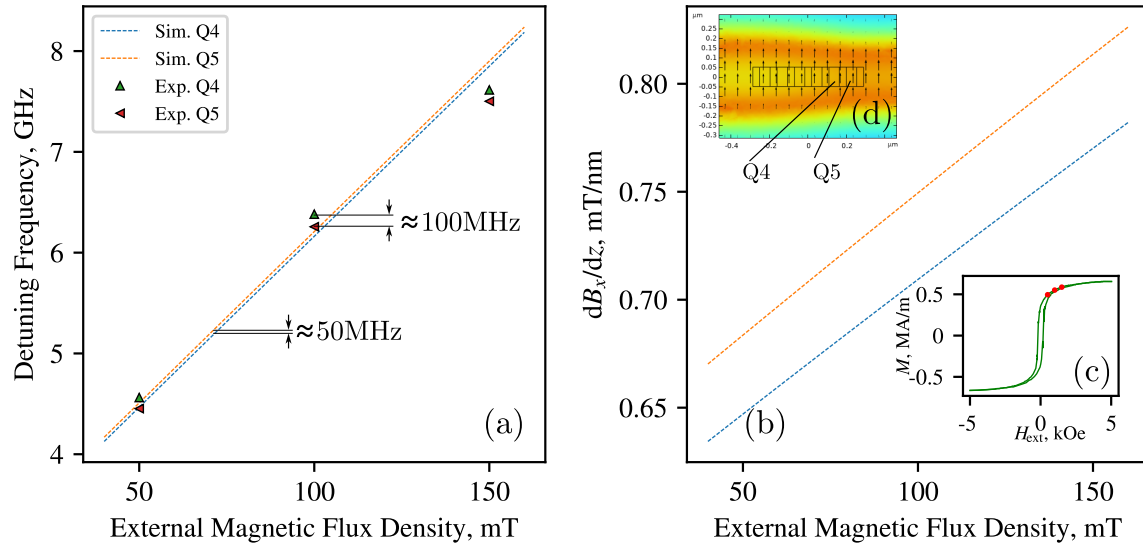


Figure 7. (a) Detuning frequency of qubits Q_1 and Q_0 , dependence on the external magnetic field. Dashed lines correspond to simulations, triangles correspond to experimental results. (b) The simulated driving gradient of corresponding qubits. (c) The hysteresis curve (green) has red dots corresponding to the measured external field. (d) Simulated net magnetic flux density with the direction of magnetic field.

Tables

Temperature	Tomography method	Reconstructed density matrix
$T = 300$ mK	Pauli decomposition	$\begin{pmatrix} 0.513e^{0.0i} & 0.030e^{-0.093\pi i} & 0.013e^{0.939\pi i} & 0.482e^{0.011\pi i} \\ 0.030e^{0.093\pi i} & 0.024e^{0.0i} & 0.021e^{-0.402\pi i} & 0.069e^{0.190\pi i} \\ 0.013e^{-0.939\pi i} & 0.021e^{0.402\pi i} & 0.020e^{0.0i} & 0.066e^{-0.303\pi i} \\ 0.482e^{-0.011\pi i} & 0.069e^{-0.190\pi i} & 0.066e^{0.303\pi i} & 0.465e^{0.0i} \end{pmatrix}$
	SPAM corrected	$\begin{pmatrix} 0.522e^{0.0i} & 0.028e^{-0.074\pi i} & 0.009e^{0.964\pi i} & 0.495e^{0.011\pi i} \\ 0.028e^{0.074\pi i} & 0.017e^{0.0i} & 0.022e^{-0.404\pi i} & 0.073e^{0.175\pi i} \\ 0.009e^{-0.964\pi i} & 0.022e^{0.404\pi i} & 0.014e^{0.0i} & 0.065e^{-0.305\pi i} \\ 0.495e^{-0.011\pi i} & 0.073e^{-0.175\pi i} & 0.065e^{0.305\pi i} & 0.467e^{0.0i} \end{pmatrix}$
	MLE (no SPAM correction)	$\begin{pmatrix} 0.508 & 0.0 & -0.002 & 0.50 \\ 0.0 & 0.0 & 0.0 & 0.0 \\ -0.002 & 0.0 & 0.0 & -0.002 \\ 0.50 & 0.0 & -0.002 & 0.492 \end{pmatrix}$
$T = 740$ mK	Pauli decomposition	$\begin{pmatrix} 0.397e^{0.0i} & 0.048e^{-0.266\pi i} & 0.061e^{0.612\pi i} & 0.347e^{0.027\pi i} \\ 0.048e^{0.266\pi i} & 0.031e^{0.0i} & 0.023e^{-0.099\pi i} & 0.082e^{0.660\pi i} \\ 0.061e^{-0.612\pi i} & 0.023e^{0.099\pi i} & 0.112e^{0.0i} & 0.107e^{-0.237\pi i} \\ 0.347e^{-0.027\pi i} & 0.082e^{-0.660\pi i} & 0.107e^{0.237\pi i} & 0.511e^{0.0i} \end{pmatrix}$
	SPAM corrected	$\begin{pmatrix} 0.530e^{0.0i} & 0.060e^{-0.258\pi i} & 0.068e^{-0.062\pi i} & 0.488e^{0.005\pi i} \\ 0.060e^{0.258\pi i} & -0.034e^{0.0i} & 0.011e^{-0.144\pi i} & 0.071e^{0.048\pi i} \\ 0.068e^{-0.062\pi i} & 0.011e^{0.144\pi i} & -0.018e^{0.0i} & 0.189e^{-0.242\pi i} \\ 0.488e^{0.005\pi i} & 0.071e^{0.048\pi i} & 0.189e^{0.242\pi i} & 0.465e^{0.0i} \end{pmatrix}$
	MLE (no SPAM correction)	$\begin{pmatrix} 0.499 & 0.001 & 0.001 & 0.50 \\ 0.001 & 0.0 & 0.0 & 0.001 \\ 0.001 & 0.0 & 0.0 & 0.001 \\ 0.50 & 0.001 & 0.001 & 0.501 \end{pmatrix}$

Table 3. Reconstructed density matrices for $|\Phi\rangle = \frac{1}{\sqrt{2}}(|00\rangle + |11\rangle)$ with and without SPAM correction using confusion matrices in Table 4. The phases in MLE results are zero.

Temperature	SPAM confusion matrix
$T = 300$ mK	$\begin{pmatrix} 0.958 & 0.008 & 0.002 & 0.039 \\ 0.007 & 0.948 & 0.043 & 0.002 \\ 0.009 & 0.015 & 0.966 & 0.001 \\ 0.027 & 0.005 & 0.012 & 0.952 \end{pmatrix}$
$T = 740$ mK	$\begin{pmatrix} 0.703 & 0.046 & 0.106 & 0.224 \\ 0.045 & 0.563 & 0.341 & 0.109 \\ 0.072 & 0.120 & 0.769 & 0.233 \\ 0.067 & 0.072 & 0.164 & 0.866 \end{pmatrix}$

Table 4. Measured SPAM confusion matrices.